
AFRL-OSR-VA-TR-2015-0085

# OPTICAL NEAR-FILED PLATES

**Roberto Merlin**
**UNIVERSITY OF MICHIGAN**

**04/08/2015**
**Final Report**



Air Force Research Laboratory
AF Office Of Scientific Research (AFOSR)/ RTD
Arlington, Virginia 22203
Air Force Materiel Command

# REPORT DOCUMENTATION PAGE

*Form Approved*
*OMB No. 0704-0188*



| **1. REPORT DATE** *(DD-MM-YYYY)* | **2. REPORT TYPE** | **3. DATES COVERED** *(From - To)* |
|---|---|---|
| 31-03-2015 | Final | 09/01/2009-12/31/2014 |

**4. TITLE AND SUBTITLE**

Optical Near-Field Plates

**5a. CONTRACT NUMBER**

**5b. GRANT NUMBER**

FA9550-09-1-0636

**5c. PROGRAM ELEMENT NUMBER**

**6. AUTHOR(S)**

erlin, Roberto, D.

**5d. PROJECT NUMBER**

**5e. TASK NUMBER**

**5f. WORK UNIT NUMBER**

**7. PERFORMING ORGANIZATION NAME(S) AND ADDRESS(ES)**

The University of Michigan
Ann Arbor, MI 48109-1120

**8. PERFORMING ORGANIZATION REPORT NUMBER**

**9. SPONSORING / MONITORING AGENCY NAME(S) AND ADDRESS(ES)**

Air Force Office of Science and Research
875 Randolph Street
Suite 325 Room 3112
Arlington, VA 22203

**10. SPONSOR/MONITOR'S ACRONYM(S)**

AFOSR

**11. SPONSOR/MONITOR'S REPORT NUMBER(S)**

**12. DISTRIBUTION / AVAILABILITY STATEMENT**

Approved for public release; distribution unlimited

**13. SUPPLEMENTARY NOTES**

**14. ABSTRACT**

Optical near-field plates were designed using antisymmetric plasmon modes to generate abrupt phase changes within a fraction of a wavelength. Plasmonic filters were developed and transmission color filtering was accomplished. The polarization property and the pitch-dependent color filtering was combined in a specially designed structure, where the polarization of light can be easily visualized. Light funneling in metallic nanostructures was studied theoretically and experimentally. We introduced a model of an aperture coupled to an oscillator that gives perfect transmission in the absence of losses. The funneling capacity of a nano-groove is slightly smaller than one wavelength. We also showed that a

**15. SUBJECT TERMS**

near-field plates; plasmonic color filtering; light funneling; transmission through subwavelength apertures; topological resonators;

| **16. SECURITY CLASSIFICATION OF:** | | | **17. LIMITATION OF ABSTRACT** | **18. NUMBER OF PAGES** | **19a. NAME OF RESPONSIBLE PERSON** |
|---|---|---|---|---|---|
| **a. REPORT** | **b. ABSTRACT** | **c. THIS PAGE** | | | Roberto D. Merlin |
| UU | UU | UU | | 15 | **19b. TELEPHONE NUMBER** *(include area code)* (734) 763-9759 |

FINAL REPORT SEPTEMBER 1, 2009 –DECEMBER 31, 2014

# OPTICAL NEAR-FIELD PLATES

Air Force Office of Scientific Research - Award Number: FA9550-09-1-0636

**Principal Investigator:**
Roberto Merlin, Professor
Physics and EECS, University of Michigan

**Co-Principal Investigator:**
L. Jay Guo, Professor
EECS, University of Michigan

## 1. PLASMONIC NEAR FIELD PLATES AT OPTICAL FREQUENCIES

We designed a near field plate (NFP) structure for deep subwavelength super-focusing at optical frequencies [1]. The method used antisymmetric surface plasmon modes to generate an abrupt π phase change within a small fraction of a wavelength, while varying the thin metallic film thickness to control the amplitude profile of the near field distribution. Numerical simulations show a λ/5 resolution at the focus for a NFP operating at the wavelength of 1550nm, which is due to the superposition of the near field phase and amplitude distribution. To produce super-focusing by using a NFP, two important requirements need to be satisfied: (*i*) alternating phase (or field polarity) between neighboring elements to remove the background field for high contrast and (*ii*) amplitude modulation of the electromagnetic field exiting the NFP. So far, the NFP concept was verified experimentally at microwave frequencies by using capacitive and inductive elements to modulate the surface impedances of a planar structure, and a focus resolution of λ/20 of the wavelength was obtained [2].

We proposed a practical design of a NFP that operates at optical frequencies by using a thin metallic film-based plasmonic structure, which explores an antisymmetric surface plasmon mode to generate the required abrupt phase modulation for super-focusing. The proposed plasmonic structure is shown in Fig. 1(a). The basic building block of the structure is illustrated in the insert of Fig. 1(b). It consists of two functional regions: a thin metallic film and a metallic slit waveguide. The function of the metallic film of varying thickness is to modulate the amplitude of the transmitted light through attenuation, and the field transmitted though the film will excite the antisymmetric surface

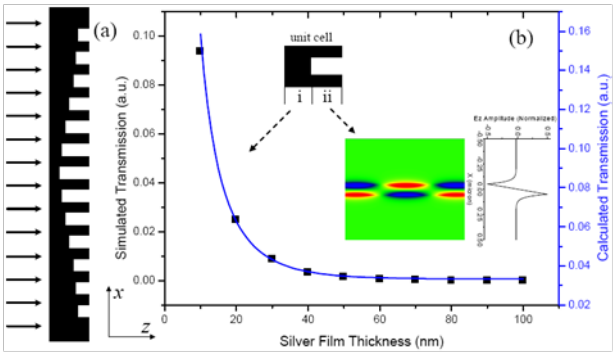


FIG. 1. (a) Schematic structure of the plasmonic NFP. (b) The principle of amplitude and phase modulation with the proposed building block that constitutes the NFP. Plotted is the transmission amplitude through the metallic film region versus its thickness. The inset shows the antisymmetric mode excited in the metallic slit structure (metal-air-metal).

plasmon mode in the metallic slit waveguide to generate a π phase difference at the opposite edge of the metallic wall. Provided that the unit cell of the structure is much smaller than a wavelength and its period is equal to the required sample interval (e.g. λ/10), the specific near field phase and amplitude distribution required for NFP can be fulfilled.

FDTD numerical simulations were performed to verify the performance of the designed NFP for TM polarized light. Fig. 2(a) shows the total electric field intensity distribution along the wave propagation path of the device, obtained by adding the $|E_x|^2$ and $|E_z|^2$ components, which clearly reveals a focus spot after the exit surface. The detailed total electric field intensity at a focal point 100 nm away from the exit surface is plotted in Fig. 2(b). It can be seen from Fig. 2(a) and 2(b) that the focus is formed as expected and with the FWHM of 300nm, i.e., λ/5. The intensities of the side lobes are relatively high as compared with the predicted ones. This is mainly due to the excitation of surface plasmons traveling along the exit surface plane. In contrast, the corresponding $|E_x|^2$ distribution presents a better focusing with very low side lobes. This design provides a convenient way to realize the NFP at optical frequencies through conventional micro-fabrication technology such as electron beam lithography and focused ion beam etch. In addition, the method can be extended to three dimensional (3D) designs to provide point super-focusing rather than the subwavelength line of the 2D case. The design strategy is very similar except that, for generating the antisymmetric mode required for NFP: in 3D super-focusing, one should employ the concentric metallic grooves in the unit cell, and set the incident light to radially polarized state to mimic the TM light for each concentric groove. Since the radially-polarized light has higher spatial symmetry than linearly polarized light, we believe that the point-focusing of the 3D case will have better resolution than the line-focusing in 2D.

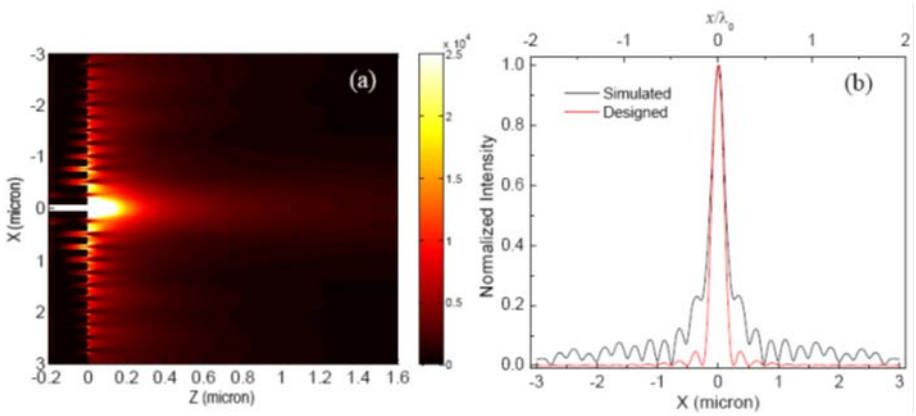


FIG. 2. (a) Total electric field intensity distribution along the wave propagation path of the NFP. (b) Cross section of the total electric field intensity at the focal plane, i.e., 100 nm away from the exit surface.

## 2. PLASMONIC FILTERS FOR SPECTRAL IMAGING

Another application of the anti-symmetric mode in a metal-dielectric (insulator)-metal (MIM) structure was developed for high resolution spectral filtering [3]. The dispersion of such a structure with proper choice of dielectric layer thickness and refractive index can provide a linear relationship between the frequency and the wave vector in the visible range. We utilized this property of the MIM stack and designed a linear array of slits that cut into the stack for the purpose of coupling incident light to the surface plasmon modes in the MIM structure (Fig. 3).

Since the structure acts as a nanoresonator and the wavelength can be selectively coupled in and scattered out of the array of resonators via the 1D grating, transmission color filtering can be accomplished, as demonstrated in Fig. 4. There are unique advantages of this physical element based color filter. First, we note that it is capable of extremely high resolution; only a few slits that cover a lateral dimension of 1μm can already show well-defined colors. Based on this finding, we demonstrated spectral dispersing with what is likely the smallest element to date; see Fig. 5(a) and (b). Another advantage is the fact that the transmitted light is naturally polarized. Thus, in the context of LCD displays, a separate polarizer sheet is not needed. In addition, light of orthogonal polarization can be reflected by the metal grating and recycled to double the transmission efficiency. The special polarization property and the pitch-dependent color filtering can be combined in a specially designed spoke structure, where the polarization state of light can be visually determined easily; Fig. 5(c) and (d). This provides an opportunity for real time polarimetric information in spectral imaging, or it can be used as a microscale polarization analyzer.

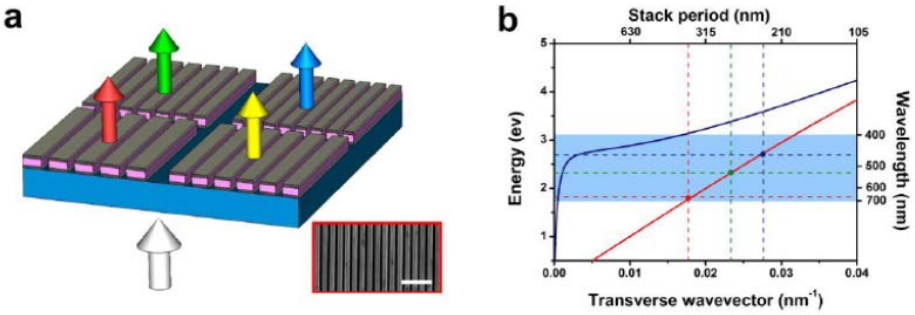


FIG. 3. (a) Schematic diagram of the proposed plamonic nano-resonators. Inset: SEM image of the fabricated device; scale bar is 1μm. (b) Plasmon dispersions in a MIM stack array. Red, green and blue dots correspond to the case of filtering primary RGB colors. Red and blue curves correspond to antisymmetric and symmetric modes, respectively.

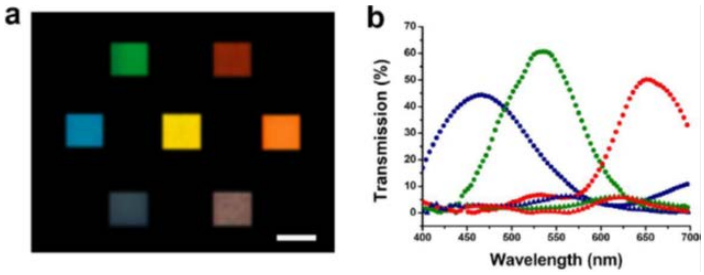


FIG. 4. (a) Optical microscopy images of seven plasmonic color filters illuminated by the white microscope light. Scale bar is 10 μm. (b) Experimentally measured transmission spectra of three fabricated color filters corresponding to the RGB colors under both TM and TE illuminations.

## 3. LIGHT FUNNELING IN PLASMONIC NANOSTRUCTURES

We have explored a new approach to focus light into deep subwavelength dimensions. The technique is capable of effectively funneling the incident light to slits of only tens of nm. Specifically we can control the light localization in a ~ 1/20 wavelength region with considerable freedom of design in both spectrum and spatial domain.

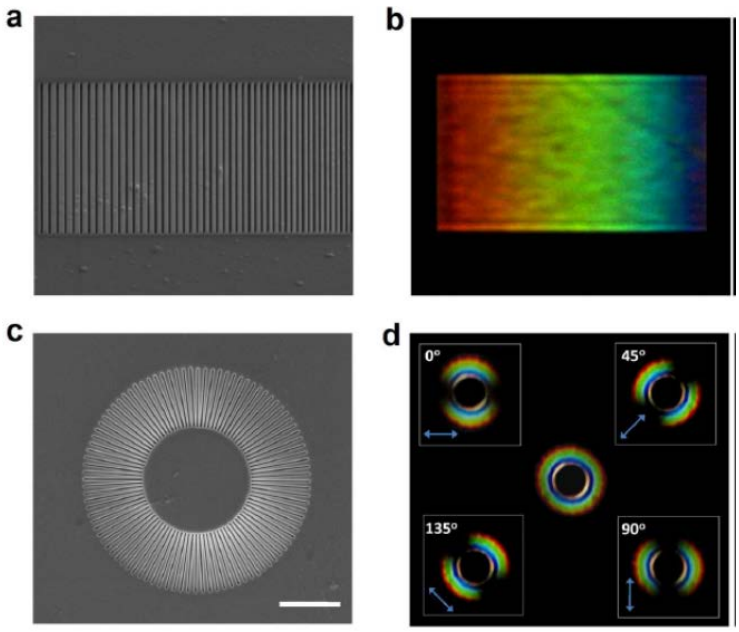


FIG. 5. (a) SEM image of the 1D plasmonic spectroscope with gradually changing periods from 400 to 200 nm (from left to right); scale bar is 2μm. (b) Optical microscopy image of the plasmonic spectroscope illuminated with white light. (c) SEM image of the fabricated 2D spoke structure. Scale bar is 3 μm. (d) Optical microscopy images of the spoken structure illuminated with unpolarized (center) and polarized light (4 boxes).

The funneling concept in plasmonic nano-grooves provides a unique way to understand the light-matter interaction in subwavelength scales, and it is believed to be responsible for the nearly perfect absorption of periodic metallic nanoslit structures. However, an outstanding question remains: is it possible for light to funnel into a single nano-groove effectively and, if so, what is the effective cross section of such funneling process? Understanding these phenomena can unambiguously determine the funneling properties in plasmonic structures and facilitate the design of plasmonic devices.

We experimentally studied the optical funneling properties of single, double and periodical nano-grooves to gain a microscopic understanding of light funneling. For a single nano-groove, we observed a pronounced funneling effect for a single nano-groove, and were able to determine the effective funneling range which is slightly smaller than the wavelength of the incident light. This allowed us to quantitatively characterize the funneling capacity of individual nano-grooves. Secondly, we studied funneling into double nano-grooves and investigated the effect of coupling between the slits. We elucidated that the coupling originates from the scattered surface wave from each groove, and established a model to reveal the underlying coupling process based on experimental results. Finally, we extended the work to periodic nano-grooves, which involve collective microscopic processes of light funneling into a single groove and coupling between double nano-grooves.

Figure 6 shows the single slit structure fabricated on a thick Au film with ultrasmooth surface to eliminate the possibility of surface plasmon excitation by surface roughness. The reflection spectra for grooves of different depths were per-

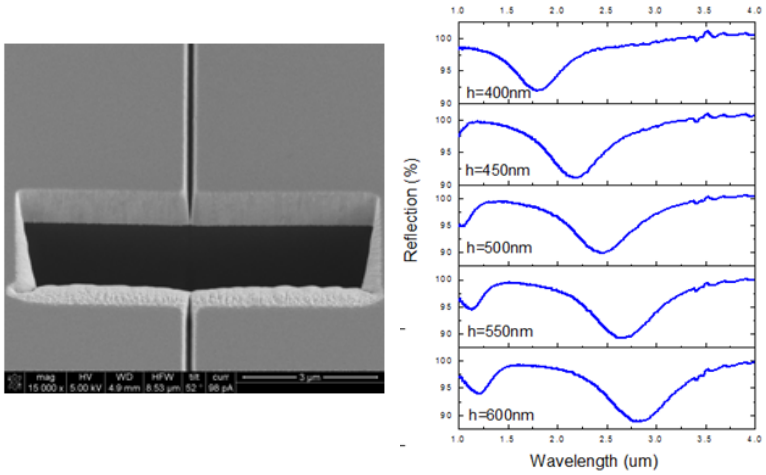


FIG. 6. Experimental structure to demonstrate funneling of light into a single plasmonic nano-groove. SEM image of the single nano-groove on ultra-flat gold film; and measured reflection spectra for different grove depths.

formed by FTIR. The results show pronounced reflection dips for single plasmonic grooves, which provides a direct evidence of the existence of resonance cavity mode in individual nano-grooves. We found that the reflection dip wavelength fulfills the condition $2\int_0^h n_{\mathrm{eff}}(x)\mathrm{d}x = (m-1/2)\lambda_m$, where $h$ is the groove depth, $m$ is an integer and $n_{\mathrm{eff}}$ is the effective index of the guided surface plasmon mode inside the nano-groove. We found that the nano-groove can absorb ~16 times more light compared with the radiation that impinges directly onto the groove opening. This means that the groove has an effective absorption cross section that is much larger than its physical size. This is the result of light funneling around the highly subwavelength structure. This observation demonstrates that light funneling can occur for a single nano-groove, without any grating structure. In order to further explore the funneling capacity, we carried out numerical simulations using COMSOL Multiphysics. This software is based on the Finite Element Method (FEM) and use TM polarized illumination. The simulated magnetic field intensity distribution reveal the first order (Figure 7a) and second order (Figure 7b) F-P resonance at the corresponding reflection dip wavelength. In Figure 7c, we plot the total electric field vectors distribution at the first-order F-P resonance wavelength of 2.93 μm. One can see that the polarized charge at the edge of metallic structure dominates the electric field distribution, creating a field profile very similar to the fringing field lines of a finite size parallel capacitor. In fact, since the structure is much smaller than a wavelength, the electrostatic approximation can be used to qualitatively understand the funneling effect. From electromagnetic point of view, the electric field distribution produced by the polarization charge can bend the energy flow characterized by the Poynting vector $\vec{S} = \vec{E} \times \vec{H}$, where the total electric field is shown in Figure 7c; the magnetic field is perpendicular to the screen. As a result, the energy flow represented by the Poynting vector is orthogonal to the contours of the electric field. This model agrees well with the simulated time averaged power flow shown in Figure 7d.

The effective funneling range deduced from the experiments clearly suggests that the funneling capacity of a nano-groove is slightly smaller than one wavelength, and that the ratio $\delta D_{\mathrm{funnel}}/\delta\lambda$ should be a universal ratio due to the scaling laws in electromagnetism. To verify this, we performed a set of measurements on nano-grooves with varying depths. Since each nano-groove has a corresponding F-P resonance wavelength, we plot the effective funneling range versus the resonance wavelength in Figure 8b. As expected, the effective funneling range increases linearly with the increase of resonance wavelength and its slop $\delta D_{\mathrm{funnel}}/\delta\lambda$ has a constant value of 0.675. This effect can explain why the reflectivity at the dip in Figure 6 decreases linearly with the increase of groove depth, since for longer resonance wavelength the effective funneling range depicted in Figure 8a is larger and therefore the reflection will decrease for a fixed incident beam width.

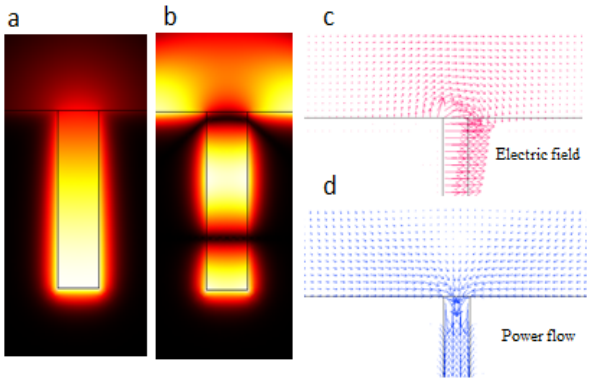


FIG. 7. (a) Simulated magnetic field intensity distribution at the first order F-P resonance wavelength of 2.93 μm. (b) Simulated magnetic intensity distribution at the second order F-P resonance wavelength. (c) Simulated electric filed vector distribution at first order F-P resonance. wavelength. (d) Simulated power flow distribution at first order F-P.

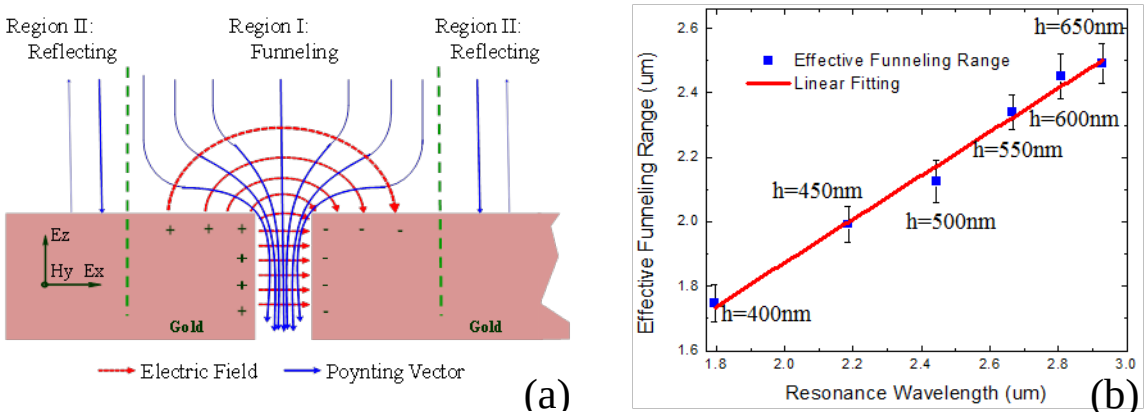


FIG. 8. Effective funneling range measurement. (a) Schematic of experiment setup and the illustrative of two functional ranges: total funneling and total reflecting. (b) Deduced effective funneling range for various grooves with different depths

We also investigated the coupling between multiple nano-grooves. We fabricated a series of double nano-groove structures with constant depth of 550 nm and varied spacing from 0.6 μm to 6.2 μm; see Figure 9(a). The reflection spectra for selected groove spacings are shown in Figure 9(b) with fixed illuminating beam width of 20 μm. When the nano-groove spacing increases from 0.8 μm to 2.8 μm, the main features of the spectra are similar to that of 550 nm single groove spectrum shown in Fig. 10(b). However, the first order F-P resonances around 2.6 μm vary in wavelength and reflectivity for different grooves spacing, which is definitely due to the coupling between the nano-grooves. To reveal the coupling mechanism, we extracted the wavelength of the first-order resonance and the corresponding reflection coefficient for every structure. Fig. 10c shows the reflectivity versus the groove spacing. This shows (1) a rapid decay at the beginning when the spacing between the two grooves increases, followed by (2) an oscillatory behavior with period of 2.7 μm, i.e., approximately one wavelength, and finally (3) saturation when the spacing between the groove is large enough. Based on these features, the reflectivity can be described by the phenomenological expression

$$R = Ae^{-Bx} + C\frac{\sin(Dx)}{x} + E \qquad (1)$$

where $x$ is the spacing between the two grooves, and $A$, $B$, $C$, $D$ and $E$ are fitting parameters with the following physical meanings:

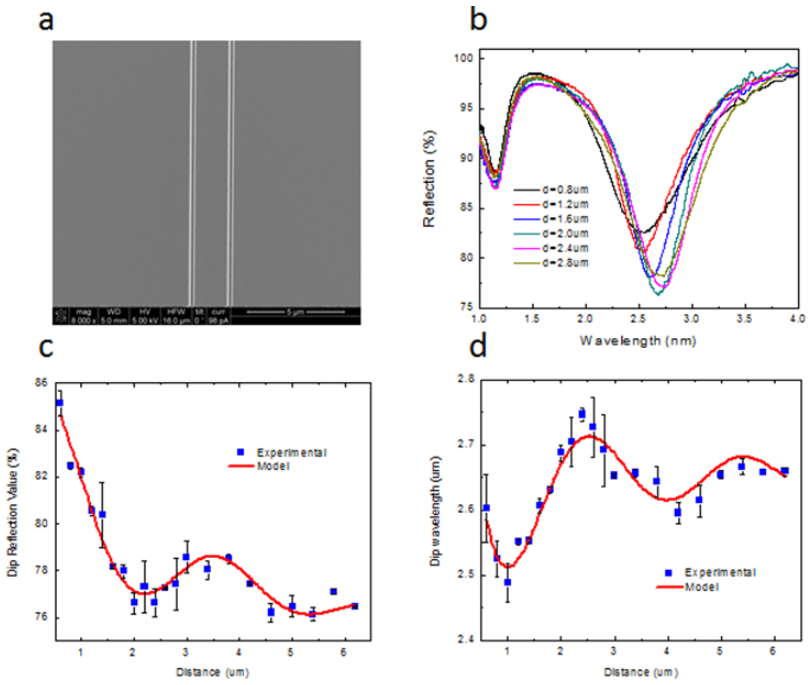


FIG. 9. Coupling between double nano-grooves. (a) SEM image of the double nano-grooves on a gold film. (b) Measured reflectivity for incident beam width of 20 μm, with various grooves spacing. (c) Minimum reflectivity value versus the grooves spacing. (d) Resonance wavelength versus the grooves spacing.

(1) the first term denotes the overlap of the two funneling regions; such overlap can reduce the effective funneling range of the system and results in decreased absorption; (2) the second term accounts for a cylindrical wave that propagates on the surface, which is generated by the scattering of nano-grooves, and the phase of the surface wave determines the constructive and destructive interference between two grooves and therefore the overall reflectivity, and (3) the third term is a constant that denotes the reflection caused by two individual nano-grooves without any coupling between them when the spacing is sufficiently large. By fitting the experimental results, we can obtain the fitting parameters. In this case, $A$= 5.27, $B$= 0.275, $C$= 2.97, $D$= 2.143 and $E$= 75.51. Based on the model proposed in Eq. (1), we can deduce that the wavelength corresponding to minimum reflectivity is the superposition of single nano-grooves and the coupling between them $\lambda_{\text{resonance}} = C\sin(dx+\phi)/x + \lambda_0$ where $\lambda_0$ is the resonant wavelength of the single nano-groove and the first term accounts for the coupling between the two grooves. In the first term, $C$ is the weight of the coupling, $d$ is related to the wave vector of the surface wave, and $\phi$ is the total phase shift cause by the scattering of the incident wave. The fitted resonance wavelength (with $c$ = 0.1536, $d$ = 2.211, $\phi$=2.085, and $\lambda_0$ =2.653) shown in Fig. 4d not only reproduces the features of the experimental data, but also matches quantitatively with each other; noting especially the matching of $d$ =2.211 in the expression for $\lambda_{\text{resonance}}$ to $D$=2.143 in Eq. (1), and $\lambda_0$ =2.653 to the dip position at large groove spacings. The physics of the coupling between the grooves and its role in determining the resonance wavelength is fairly clear from this analysis. Finally to understand the behavior of light funneling on geometry, we fabricated circular groves. The observations summarized in Fig. 10 are consistent with those for linear slits.

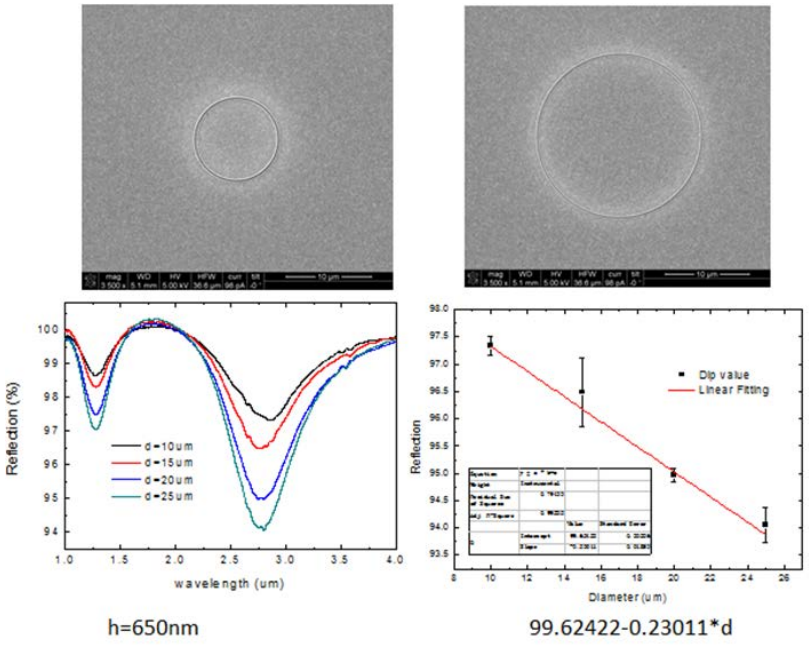


FIG. 10. Funneling in circular nanogroves fabricated in Au films.

## 4. IMAGING WITH A MAXWELL FISH-EYE LENS

Maxwell's fish eye lens [4] is a sphere of radius $R$ for which the refractive index varies according to

$$n(r) = \frac{2}{1+(r/R)^2} \qquad (2)$$

where $r$ is the distance from the center of the sphere. Inside the lens, rays paths are circles and all rays from an object at $\mathbf{r}_O$ converge at the image point at $\mathbf{r}_I = -\mathbf{r}_O R^2 / |\mathbf{r}_O|^2$ [4]. The fish-eye lens has recently attracted much attention,

motivated by claims that it provides perfect imaging of electromagnetic waves, in an apparent violation of Abbe's diffraction limit [5]. In a series of papers [6,7,8,9,10.11], Leonhardt *et al*. have argued that the mirrored fish-eye gives unlimited resolution in two [6] and three dimensions [7], and responded to comments by Blaikie [12], Kinsler and Favaro [13] and Merlin [14], who questioned various aspects of their proposal, particularly in regard to the meaning of electromagnetic drains [6,7,8], causality [8,14], image perfection [10,11], and the assertion that time-reversed sources can be represented by passive outlets [10]. We note that, using transformation optics methods, Benítez et al. [15] reached conclusions similar to those of Leonhardt *et al*. for scalar fields in lensing systems other than Maxwell's fish-eye, whereas Guenneau *et al*. failed to observe deep subwavelength resolution in both Maxwell's fish-eye and the Eaton lens [16].

We compared Maxwell's fish eye to the mathematically simpler problem of a spherical mirror, and find strong similarities in their imaging behavior. We used this analogy to show that the perfect focusing claimed by Leonhardt *et al*. [6,7] is not an intrinsic property of the fish eye lens, but merely the result of having placed an additional source at the image position. In this regard, their proposal is reminiscent of schemes relying on time-reversed sources to attain subwavelength focusing [17,18]. The extra source leads to a resulting field pattern that imitates the behavior of a drain; see Fig. 11. Leonhardt *et al*. assert that drains are necessary to achieve a stationary state and that solutions without them violate causality [7]. In contrast, we find that the problem of a single dipole in an ideal spherical cavity does exhibit causal stationary states without the need for drains, and that the images obtained in that situation obey Abbe's constraint. Disproving the belief that mirrors are not good analogues of Maxwell's lens [10,11] our analysis shows that, as for the dispersionless fish eye, electromagnetic pulses do not experience shape distortion as they propagate in large spherical cavities. Finally, we showed that passive outlets can imitate drains, but only at a single frequency (this is consistent with recent study by Kinsler [19]) and under conditions that require fine tuning of parameters.

Finally, we discussed the possibility that time-reversed sources may be replaced by passive outlets, addressing the claim by Leonhardt *et al*. [6] that Maxwell's fish eye makes a perfect lens for electromagnetic waves but only when such waves are detected by perfect point detectors." As we have shown, the spherical mirror has properties similar to those of the fish-eye lens. Can a passive detector at the origin lead to behavior that imitates a drain in the spherical mirror? As recent work has shown for the general case [19], the answer is yes, but only at a single predetermined frequency. Here, we give an alternative argument. Detectors of dimensions $\sim \ell$ that are small compared with the wavelength $\lambda$ behave as particles in a uniform field [20]. Let $p_{\mathrm{D}}$ be the electric dipole acquired by the detector and $\gamma_{\mathrm{D}}$ its electrical polarizability (we ignore magnetic effects). A calculation of the field at the origin, due to the induced currents at the mirror, gives $\mathbf{E}(0) = E(0)\mathbf{e}_z$ where $E(0) = (2i/3)Ak^3(p_0 + p_{\mathrm{D}})$. A perfect drain-like pattern requires that $p_{\mathrm{D}} = \gamma_{\mathrm{D}} E(0) = -p_0 e^{i\Phi}$ which gives

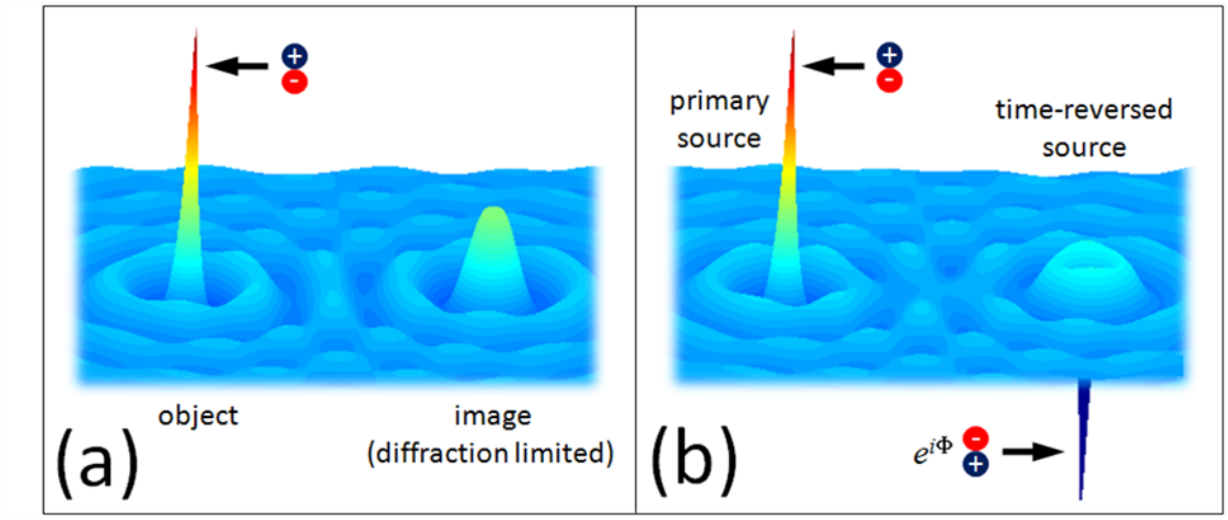


FIG. 11. A cartoon view of imaging in Maxwell's fish eye and ellipsoidal mirrors. (a) A single dipole source gives diffraction limited focusing. (b) The result of adding a second, time-reversed electric dipole at the position of the image is a field pattern that emulates that of a drain.

$$\gamma_D = 3i/4k^3. \qquad (3)$$

Since the polarizability is proportional to the volume of the detector, it is clear that this condition together with $\ell << \lambda$ can only be met in the vicinity of a high-*Q* resonance and at a single frequency. As an example, if we model the outlet as a sphere of radius $r_D$ and permittivity $\varepsilon_D$, the polarizability is $\gamma_D = (\varepsilon - 1)r_D^3/(\varepsilon + 2)$ [20], and the relevant resonance is that of the so-called surface plasmon. Thus, the condition set by Eq. (3) reads $\varepsilon_D \approx -2 + 4ik^3 r_D^3$. Similar considerations apply to the microwave experiments reported by Ma *et al.* [21] in which the outlets were absorbers identical to the source and impedance-matched to the cables, which behaved as sources in reverse. It is important to note that, even if passive elements could be used for broadband operation, their associated drains would not provide subwavelength resolution. The reason is that the spatial dependence of the amount of radiation emitted or absorbed by the device would still be limited by diffraction effects and, as such, by the same signal-to-noise problems that arise when trying to resolve objects whose separation is smaller than that allowed by Abbe's formula.

## 5. TRANSMISSION OF WAVES THROUGH SMALL APERTURES

It has been known for a long time that small holes, of dimensions $\ell$, are ill suited for transmitting electromagnetic, acoustic or other disturbances of wavelength $\lambda$. The normalized transmittance, $T_N$, *i. e.*, the ratio between the power transmitted and that incident upon the hole, is $\sim(\ell/\lambda)^4$. More recently, Ebbesen *et al.* [22] showed that periodic arrays of small apertures in a metallic film can lead to an extraordinary enhancement of the optical transmission. This important discovery has led to numerous ideas for applications in areas such as sensing, near-field microscopy and light harvesting, that can benefit from the concurrent enhancement of the electric field in the vicinity of the apertures.

The mechanisms underlying extraordinary transmission for hole arrays are fairly well understood. In particular, the distinct and cooperative roles played by surface modes (plasmon polaritons) and waveguide or Fabry-Pérot-type resonances are now well established; see: F. J. García-Vidal *et al.* [23]. The same cannot be said for single apertures. While the utilization of geometric and plasmon resonances to enhance the transmission of small, isolated openings has been considered before, a unified physical picture has not yet emerged. We introduced a simple yet comprehensive model of a closed-curve aperture coupled to an oscillator that gives perfect transmission, that is, $T_N \sim (\ell/\lambda)^2$, in the absence of all but radiative losses [24]. The model draws from ideas that have been hinted at but not fully treated in the engineering literature. It applies to openings in resonant cavities as well as to approaches involving *LC* and other geometric resonances for which the resonant wavelength decreases with the size of the aperture. We also give an example of resonant transmission through apertures with open-curve boundaries, which relies on the interaction with a localized TE state bound to a pair of pinholes in a two-dimensional waveguide [24]. This problem is related to the so-called single-slit funneling [25] in that the key resonance is of the Fabry-Pérot type but, unlike funneling, the transmittance does not decrease with decreasing slit width and exactly matches the incident power for arbitrarily small hole sizes [26]. In funneling and related cases, we find that resonant coupling to waveguide modes gives imperfect transmission, with transmitted powers that are on the order of those for single slits off-resonance.

In a series of experiments, we showed that a pair of subwavelength slits in parallel conducting plates supports a localized electromagnetic mode bound to the slits, whose spatial extent is determined not by the plates' size but by the slit dimensions; see Figure 12. This mode occurs for electric fields parallel to the slits and plate separation slightly smaller than half the free-space wavelength. Finite element calculations and experimental results at 10 GHz show that the localized mode gives rise to a strong, narrowband resonant enhancement of the transmission which, while limited by conduction losses in the plates, is a factor of $10^4$ larger than for off-resonant transmission.

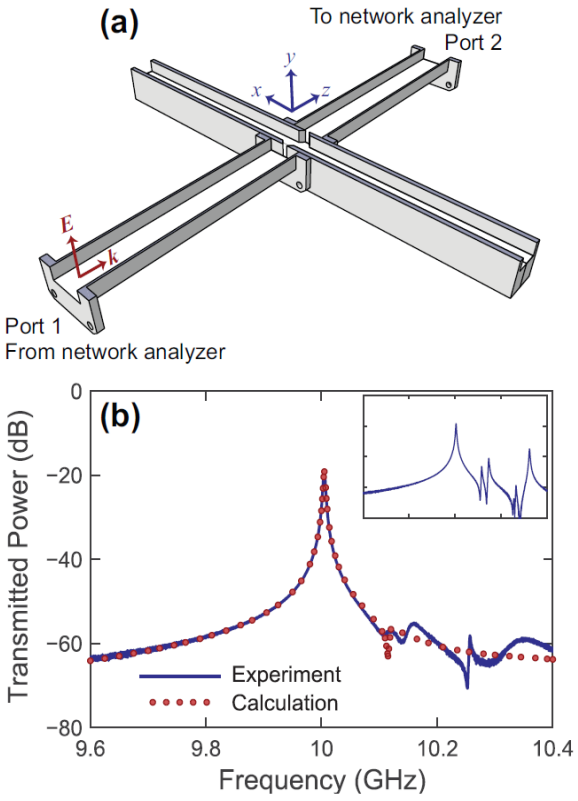


FIG. 12. (a) Drawing of the aluminum cavity and waveguides used in the experiment. For clarity, the upper ground plane at y = h is not shown. (b) Measured (blue line) and calculated (red dots) power transmission coefficient from port 1 to port 2. (inset) Measured transmission when the open cavity ends are covered with conducting plates.

## 6. TOPOLOGICAL ELECTROMAGNETIC RESONATORS

Resonant cavities (RCs) are devices used to confine light or other wave disturbances. They are broadly characterized by a set of quality factors *Q*, defined as the ratio between the frequency ω and the width $\delta\omega$ of a particular mode, and finesses $F = \Delta\omega / \delta\omega$, where Δω is the separation between adjacent modes. The most common implementation of a RC involves a region defined by a mirrored surface. Mirrorless RCs are also well known. Examples include natural substances which rely either on total internal reflection to give confinement close to the boundary (as for whispering gallery modes [27]) and systems sustaining modes that lie outside the light cone such as, e. g., surface plasmons in metals. We have shown [28] that, in a narrow range of allowed frequencies, photonic crystals (PCs) [29] behave as mirror-free RCs regardless of their shape (this is unlike PC cavities resulting from defects, which operate at frequencies inside forbidden gaps [30]). Ignoring all but radiative losses, and for arbitrary dimensions, the corresponding states are surface-avoiding [31], extended modes that lie inside the light cone, with *Q* values on the order of $(L/\lambda)^3$ and $F \sim L/\lambda$, where λ is the wavelength in vacuum and $L >> \lambda$ is a typical length of the PC. Analogous results apply to plasmonic materials just above the plasmon frequency.

The results in Fig. 13, for a square lattice of rods of radius *r* and lattice parameter *a*, illustrate the topological properties of a PC resonator. The permittivity of the host (rods) is $\varepsilon_1$ ($\varepsilon_2$). A plane wave with electric field perpendicular to the page impinges on the PC from the left. Fig. 13(b) and (c) show, respectively, the calculated absorption for the cases where the PC outer boundary is a circle and a bow tie The frequency range shown is in the vicinity of a band edge at the M point of the Brillouin zone. The PC parameters are such that there is an optical gap in the range $\omega_G \approx 0.28 \lesssim \omega a / 2\pi c \lesssim 0.42$. The surface-avoiding, cavity modes manifest themselves as the narrow peaks which occur below and near the edge of the allowed band, at $\omega \lesssim \omega_G$, where the *q*-dependence of ω is quadratic. Contour plots of the field magnitude are shown for the two highest-lying modes (i) and (ii). It is apparent that their envelopes are in a one-to-one correspondence with the profiles of a mirrored RC, which can be ordered according to the number of

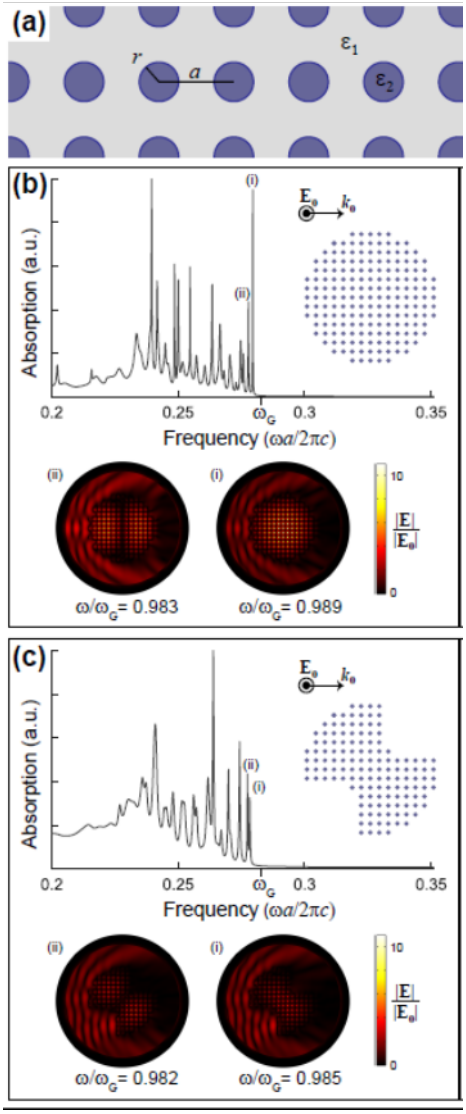


FIG. 13. Results for a square lattice of rods. (a) Parameters are $\varepsilon_1$=1, $\varepsilon_2$=12×(1+0.0001*i*) and *r*/*a* = 0.2. Absorption data for a finite PC defined by (b) a circle and (c) a bow tie.

zeros of the Dirichlet eigenfunctions. An analysis of these results show that the frequency separation between two arbitrary peaks and their width scale, respectively, like $D^{-2}$ and $D^{-3}$, where $D$ is the radius of the circle for (b) and an arbitrary length of the bow tie for (c).

Surface-avoiding modes occur also in homogeneous substances and, in particular, plasmonic media immediately above the plasmon frequency where 0<Re(ε)<<1. With some modifications, the general analysis [28] can be applied to such systems. Inasmuch as the PC problem is the optical counterpart to that of a quantum particle in a periodic potential, the plasmonic problem is analogous to that of a particle in the piecewise constant potential $V = V_0 > 0$ and $V = 0$ inside and outside $\Xi$, respectively. Consider now a plasmonic substance whose permittivity is given by

$$\varepsilon = \varepsilon_\infty + \frac{\omega_0^2 (\varepsilon_0 - \varepsilon_\infty)}{\omega_0^2 - \omega^2 + i\omega\gamma} \quad , \tag{4}$$

where $\varepsilon_0$ and $\varepsilon_\infty$ are, respectively, the static and high-frequency dielectric constants, $\omega_0$ is the frequency and γ is the full width of the resonance. Close to Re(ε) = 0, and for $\gamma << \omega_0$, the dependence of the frequency on the wavevector is of the form $\omega \approx \omega_P + Aq^2$ where $A$ is a constant and $\omega_P$ is the plasma or longitudinal-optical phonon frequency. Thus $v_G, n_\Xi \propto L^{-1}$ and, as for PCs, we get that $\delta\omega/\omega \sim \lambda^3 / L^3$.

Exact results support the existence of long-lived RC modes in plasmonic systems. Fig. 14 shows absorption by a sphere of radius $R$ made of a substance whose permittivity is given by Eq. (4). Curves were calculated using the exact expressions for Mie scattering [32]. The extended modes that set the sphere as a RC manifest themselves as the narrow peaks that occur just above $\omega_P$. As expected, the two lowest eigenmodes depicted in Fig. 14(b) show vanishing intensity at the surface of the sphere. As for PCs, the results at various radii shown in Fig. 14(c) indicate that the distance between peaks scales like $R^{-2}$ and that the widths of the peaks decrease as $R^{-3}$ with increasing radius. The latter behavior persists until one reaches the point where the radiative width becomes smaller than the non-radiative one after which the peak intensity diminishes strongly.

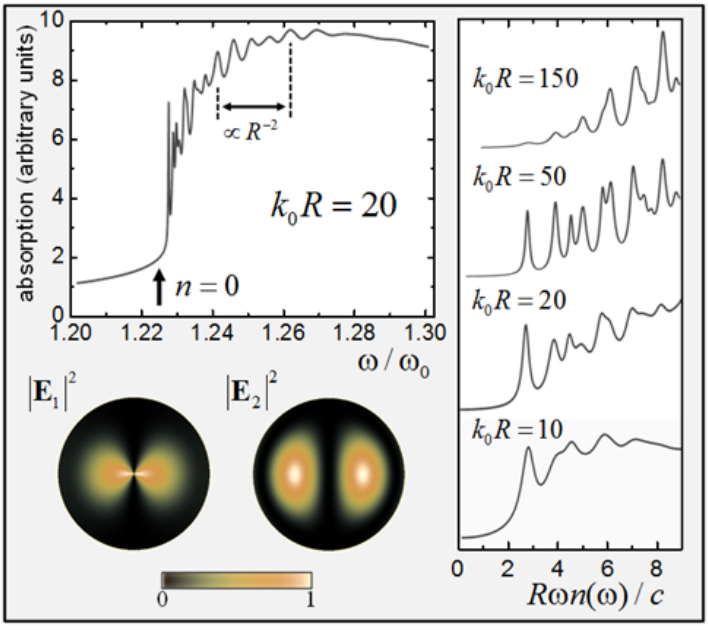


FIG. 14. (a) Absorption data for a sphere of radius $R$ and permittivity given by Eq. (5); $k_0 = \omega_0/c$. (b) Contour plot of the electric field intensity for the two lowest eigenmodes. (c) Absorption as a function of for various radii. Parameters are $\varepsilon_0$=3, $\varepsilon_\infty$=2 and $\gamma/\omega_0 = 10^{-4}$.

## 7. PERSONNEL SUPPORTED

| co-PIs | Graduate Students | Postdoctoral Fellows |
|---|---|---|
| L. Jay Guo | Haofei Shi | Taehee Jang |
| Roberto Merlin | Ting Xu | Jing Zhou |
| | Yihuei Wu | Haofei Shi |
| | Ilya Vugmeister | |
| | Meredith Henstridge | |
| | Steve Young | |

## 8. PUBLICATIONS


1. R. Merlin, "Metamaterials and the Landau-Lifshitz Permeability Argument: Large Permittivity Begets High-Frequency Magnetism." *Proc. Nat. Acad. Sci.* **106**, 1693-1698 (2009).
2. T. Xu, Y.-K. Wu, and X.-G. Luo and L. J. Guo, "Plasmonic nano-resonators for color filtering and spectral imaging," *Nat. Comm.* **1**, 59 (2010).
3. H.-F. Shi and L. J. Guo, "Design of Plasmonic Near Field Plate at Opitical Frequency," *Appl. Phys. Lett.* **96**, 141107, (2010).
4. R. Merlin, "Comment on 'Perfect imaging with positive refraction in three dimensions'." *Phys. Rev. A* **82**, 057801 (2010).
5. R. Merlin, "Maxwell's Fish-Eye Lens and the Mirage of Perfect Imaging," *J. Opt.* **13**, 024017 (2011); invited paper in a special issue on Transformation Optics, ed. by J. B. Pendry and V. M. Shalaev.
6. H.-F. Shi, J. G. Ok, H. W. Baac, L. J. Guo, "Low density carbon nanotube forest as an index-matched and near perfect absorption coating," *Appl. Phys. Lett.* **99**, 211103 (2011).
7. T. Xu, H.-F. Shi, Y.-K. Wu, A. F. Kaplan, J. G. Ok, and L. J. Guo, "Structural Colors: from Plasmonic to Carbon Nanostructures," *Small*, **7**, 3128–3136 (2011).
8. A. Grbic, R. Merlin, E. M. Thomas and M. F. Imani, "Near-Field Plates: Metamaterial Surfaces/Arrays for Sub-wavelength Focusing and Probing." *Proc. IEEE* **99**, 1806-1815 (2011), invited paper in a special issue on Metamaterials, ed. by G. V. Eleftheriades and N. Engheta.
9. R. Merlin, "Pinholes Meet Fabry-Pérot: Perfect and Imperfect Transmission of Waves Through Small Apertures," *Phys. Rev. X* **2**, 031015 (2012).
10. I. D. Vugmeyster, J. F. Whitaker and R. Merlin, "GaP based terahertz time-domain spectrometer optimized for the 5-8 THz range," *Appl. Phys. Lett.* **101**, 181101 (2012).
11. Y.-K. Wu, A. E. Hollowell, C. Zhang, L. J. Guo, "Angle-Insensitive Structural Colours based on Metallic Nanocavities and Coloured Pixels beyond the Diffraction Limit," *Scientific Reports*, **3**, 1194, (2013).

12. S. M. Young, C. Pfeiffer, A. Grbic and R. Merlin, "Enhanced resonant transmission of electromagnetic radiation through a pair of subwavelength slits," *Appl. Phys. Lett.* **103**, 041104 (2013).

13. R. Merlin and S. M. Young, "Photonic Crystals as Topological Resonators," *Opt. Express* **22**, 18579-18587 (2014).

14. T.-H. Jang, H. Youn. Y. J. Shin. L. J. Guo, "Transparent and Flexible Polarization-Independent Microwave Broadband Absorber," *ACS Photon.* **1**, 279–284 (2014).

15. S. L. Chen, Y.-C. Chang, C. Zhang, J. G. Ok, T. Ling, M. T. Mihnev, T. B. Norris, L. J. Guo, "Efficient real-time detection of terahertz pulse radiation based on photoacoustic conversion by carbon nanotube nanocomposite," *Nat. Photon.* **8** (7), 537-542 (2014).

16. J. Zhou, and L. J. Guo, "Transition from a spectrum filter to a polarizer in a metallic nano-slit array," *Sci. Rep.* **4**, 3614 (2014).

## 9. PATENT DISCLOSURES

none

## 10. HONORS AND AWARDS

Roberto Merlin is the Peter A. Franken Professor of Physics, University of Michigan. He is a Fellow of the American Physical Society, the Optical Society of America, the American Association for the Advancement of Science, the von Humboldt Foundation, the Simons Foundation and the John Simon Guggenheim Memorial Foundation. Other honors include the 2006 Frank Isakson Prize of the American Physical Society for Optical Effects in Solids and Lannin Lecturer (2002) at the Department of Physics, Pennsylvania State University.

## 11. REFERENCES

[1] H.-F. Shi and L. J. Guo, *Appl. Phys. Lett.* **96**, 141107 (2010).

[2] A. Grbic, L. Jiang and R. Merlin, *Science* **320**, 511 (2008).

[3] T. Xu, Y.-K. Wu, and L. J. Guo, *Nat. Comm.* **1**, 59 (2010).

[4] C. M. Maxwell, *The Scientific Papers of James Clerk Maxwell*, edited by W. D. Niven, Vol. 1 (Dover Publications, New York, 1952), p. 76. The fish-eye lens is mentioned for the first time in a problem [Cambridge & Dublin Math. J. **8**, 188 (1853)] and its solution [*ib*. **9**, 9 (1854)], both attributed to Maxwell.

[5] E. Abbe, *Arch. Mikrosk. Anat.* **9**, 413 (1873).

[6] U. Leonhardt, *New J. Phys.* **11**, 093040 (2009).

[7] U. Leonhardt and T. G. Philbin, *Phys. Rev. A* **81**, 011804 (R) (2010).

[8] U. Leonhardt, *New J. Phys.* **12**, 058002 (2010).

[9] U. Leonhardt, *arXiv*:1010.4161.

[10] U. Leonhardt and T. G. Philbin, *Phys. Rev. A* **82**, 057802 (2010).

[11] U. Leonhardt and S. Sahebdivan, *J. Opt.* **13**, 024016 (2011).

[12] R. J. Blaikie, *New J. Phys.* **12**, 058001 (2010).

[13] P. Kinsler and A. Favaro, *New J. Phys.* **13**, 028001(2011).

[14] R. Merlin, *Phys. Rev. A* **82**, 057801 (2010).

[15] P. Benítez, J. C. Miñano and J. C. González, *Opt. Express* **18**, 7650 (2010).

[16] S. Guenneau, A. Diatta and R. C. McPhedran, *J. Mod. Opt.* **57**, 511 (2010).

[17] G. Lerosey, J. de Rosny and M. Fink, *Science* **315**, 1120 (2007).

[18] J. de Rosny and M. Fink, *Phys. Rev. Lett.* **89**, 124301 (2002).

[19] P. Kinsler, *Phys. Rev. A* **82**, 055804 (2010).

[20] L. D. Landau and E. M. Lifshitz, *Electrodynamics of Continuous Media* (Pergamon, Oxford, 1960), p. 319.

[21] Y. G. Ma, C. K. Ong, S. Sahebdivan, T. Tyc and U. Leonhardt, *New J. Phys.* **14**, 025001 (2012).

[22] T. W. Ebbesen, H. J. Lezec, H. F. Ghaemi, T. Thio, and P. A. Wolff, *Nature* **391**, 667 (1998).

[23] F. J. García-Vidal, L. Martin-Moreno, T. W. Ebbesen and L. Kuipers, *Rev. Mod. Phys.* **82**, 729 (2010).

[24] R. Merlin, *Phys. Rev. X*, **2**, 031015 (2012).

[25] F. Pardo, P. Bouchon, R. Haïdar and J. L. Pelouard, *Phys. Rev. Lett.* **107**, 093902 (2011).

[26] The localized mode is robust in that simulations using commercially available software indicate its persistence in structures made of real metals all the way into the optical range as well as for perfectly conducting screens with thickness $<< \lambda$.

[27] A. B. Matsko and V, S. Ilchenko, *IEEE J. Select. Topics Quantum Electron*. **12**, 3 (2006).

[28] R. Merlin and S. M. Young, *Optics Express* **22**, 18579 (2014).

[29] E. Yablonovitch, *Phys. Rev. Lett.* **58**, 2059 (1987); S. John, *Phys. Rev. Lett*. **58**, 2486 (1987).

[30] Y. Akahane et al., *Nature* **425**, 944 (2003).

[31] R. Merlin, *Phil. Mag. B* **70**, 761 (1994).

[32] See: C. F. Bohren and D. R. Huffman, *Absorption and Scattering of Light by Small Particles* (Wiley, New York, 1983), Ch. 4.